**Proceedings Paper:**
Greenidge, N.J., Marzi, C., Calmé, B. et al. (2025) Designing a Magnetic Endoscope for In Vivo Contact-Based Tissue Scanning Using Developable Roller. In: Proceedings of 2025 IEEE/RSJ International Conference on Intelligent Robots and Systems (IROS). 2025 IEEE/RSJ International Conference on Intelligent Robots and Systems (IROS), 19-25 Oct 2025, Hangzhou, China. Institute of Electrical and Electronics Engineers (IEEE), pp. 32-37. ISSN: 2153-0858. EISSN: 2153-0866.

https://doi.org/10.1109/iros60139.2025.11247414

# Designing a Magnetic Endoscope for In Vivo Contact-Based Tissue Scanning Using Developable Roller

Nikita J. Greenidge[1], Christian Marzi[2,3], Benjamin Calmé[1], James W. Martin[1], Bruno Scaglioni[1], Franziska Mathis-Ullrich[3], *Member*, IEEE, and Pietro Valdastri[1], *Fellow*, IEEE

***Abstract*— Magnetic manipulation has been adopted as a method of actuation in both wireless capsule endoscopy and soft-tethered endoscopy, with the goal of improving gastrointestinal procedures. However, by nature of magnetic manipulation, these endoscopes are typically limited to a maximum of five degrees of freedom (DoF). With the need to introduce additional contact-based sensing modalities for subsurface investigation into these systems as well as to improve overall dexterity, it is both practically and clinically beneficial to recover the lost DoF i.e. the roll around the main axis. This paper presents a method of achieving the magnetic manipulation of an underactuated device by leveraging developable surfaces, specifically, the oloid shape. The design of a clinically relevant magnetic endoscope with all its ancillary elements, as well as contact sensors, is proposed and demonstrated in vivo. The contact sensor data from the in vivo experiments show that for sweeping motions over 100° of roll, contact between the endoscope's sensor region and the colon wall can be maintained for 74% of the motion.**

## I. Introduction

Gastrointestinal (GI) cancers, particularly in the colon, stomach, and esophagus, account for 18.7% of new cancer cases and 22.6% of cancer-related deaths globally [1]. These slow-progressing diseases have a prolonged asymptomatic phase [2], making early detection through screening essential. Conventional flexible endoscopy (FE) is the gold standard for visualization, but its push-driven mechanism often causes pain, requires sedation, and risks perforation. Key clinical challenges include improving patient comfort, enhancing adenoma detection, and expanding diagnostic and therapeutic capabilities [3].

Capsule endoscopy, first introduced as an ingestible pill-sized camera [4], has since evolved into actively manipulated tethered and untethered systems. Magnetic actuation has demonstrated 5-degree-of-freedom (DoF) control in both categories [5]–[7], enabling front-driven propulsion with reduced patient discomfort and lower procedural risks. Additionally, real-time localization and automation [8] can ease operator workload and reduce training time.

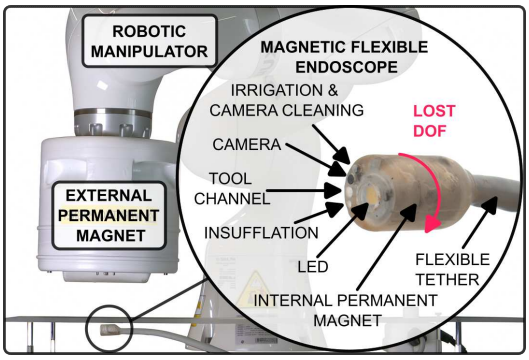


Fig. 1. **Overview of the magnetic flexible endoscope (MFE) system:** Illustration of the "lost DoF" in magnetic manipulation and key elements.

Magnetic manipulation relies on external fields to generate forces and torques on an embedded magnetic element. The commonly used magnetic dipole model describes this interaction, where the device aligns with the field to minimize potential energy. A fundamental limitation of this approach is the inability to induce torque around the magnetization axis (see "Lost DoF" in Figure 1), restricting full dexterity. This affects precise tool positioning for biopsy and therapy, as well as the integration of advanced sensing modalities.

Previous work using the Magnetic Flexible Endoscope (MFE) [9] demonstrated micro-ultrasound imaging within the GI tract but remained constrained by 5-DoF control, limiting image acquisition quality. Solutions such as mechanically rotating transducers [10], [11] add mechanical complexity without addressing overall dexterity. Meanwhile, standard FE has reported adenoma miss rates up to 30% [12], particularly for flat or right-sided lesions. While enhanced optical techniques such as narrowband imaging (NBI) and chromoendoscopy [13] improve mucosal visualization, subsurface imaging methods like micro-ultrasound ($\mu$US) [14], Optical Coherence Tomography (OCT) [15], photoacoustics [16] and Terahertz imaging [17] are necessary for in situ histological assessment.

Recovering roll control is critical before integrating additional sensing modalities. This work explores a novel underactuated approach that exploits endoscope-tissue interactions to restore roll motion using only external magnetic actuation. By leveraging differential geometric principles, we intro-

[1]N.J. Greenidge, B. Calmé, J.W. Martin, B. Scaglioni, and P. Valdastri are with the STORM Lab, Institute of Autonomous Systems and Sensing (IRASS), School of Electronic and Electrical Engineering, University of Leeds, UK. Corresponding author: elnjg@leeds.ac.uk (N.J. Greenidge)

[2]C. Marzi is with the Institute for Anthropomatics and Robotics, Karlsruhe Institute of Technology, Karlsruhe, Germany.

[3]C. Marzi and F. Mathis-Ullrich are with the Surgical Planning and Robotic Cognition Lab, Friedrich-Alexander-Universiät Erlangen-Nürnberg, Erlangen, Germany.

This work was supported in part by the European Research Council (ERC) through the European Union's Horizon 2020 Research and Innovation Programme under Grant 818045, in part by the European Commission (EC) through Horizon 2020 Research and Innovation Programme under Grant 952118, and in part by the Engineering and Physical Sciences Research Council (EPSRC) under Grant EP/V047914/1. Any opinions, findings and conclusions, or recommendations expressed in this article are those of the authors and do not necessarily reflect the views of the ERC, the EC or the EPSRC.

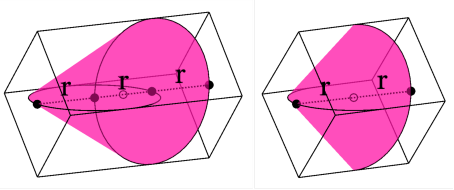


Fig. 2. Convex hull and bounding box of the Oloid (left) and the sphericon (right) where $r$ is the radius of the forming circles.

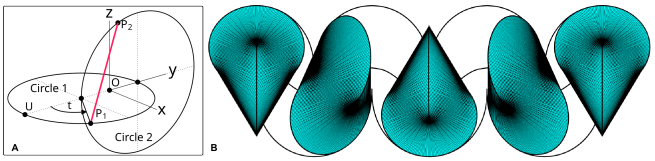


Fig. 3. **The oloid:** (**A**) Geometric representation with generator line in red and (**B**) Rolling motion with generator lines shown in black. Adapted from [19].

duce a developable roller design, where controlled pitching and yawing induce continuous roll motion. This method maintains low power consumption, lightweight design, and reduced mechanical complexity while improving diagnostic and therapeutic precision.

## II. Methods

### A. Choosing the Right Developable Roller

Most developable rollers are characterized by their ability to develop their entire surface while rolling and possess the property of keeping their center of mass at a constant height. The oloid has some unique characteristics which set it apart from the rest of its developable roller family, but, it is most closely related to the sphericon as both can be generated by calculating the convex hull of circular arcs (as shown in Figure 2). A side-by-side geometric comparison of the sphericon and the oloid is summarized in Table I.

For scopes used in the GI tract, the limiting dimensions are those of the cross-section across the transverse plane as this determines ease and therefore comfort of insertion and manipulation. Due to the long tubular form factor of the majority of the tract, endoscopes can acceptably have rigid lengths of up to 30 mm for upper GI and 60 mm for lower GI [18] to be considered a clinically relavant size. This means that for the same cross-sectional dimensions (r), the oloid shape provides more space for internal components, especially those with cylindrical form factor. One other unique feature of the oloid is that it has zero vertices compared to the 4 of the sphericon which means that in applications where sharp edges are to be avoided in order to reduce damage to tissue, the oloid is favorable. For these reasons the oloid was chosen as the developable roller for this demonstration of roll recovery in magnetic endoscopes.

TABLE I

Properties of the Oloid and the Sphericon

| Property | Oloid | Sphericon |
|---|---|---|
| Angle of inclination | $30°$ | $45°$ |
| Length of generator | $\sqrt{3}r$ | $\sqrt{2}r$ |
| Number of vertices | 0 | 4 |
| Number of edges | 2 | 2 |
| Internal volume | $3.0524r^3$ | $2.0943r^3$ |
| Cross-section | $2r^2$ | $2r^2$ |
| Length | $3r$ | $2r$ |
| Overall volume | $5.9921r^3$ | $3.9921r^3$ |
| Volume ratio | 0.509 | 0.525 |

### B. Geometrical Description of the Oloid

The meandering motion of the oloid, shown in Figure 3 demonstrates the coupling of pitch and yaw movement with its movement in the roll direction. This way, in a system where roll is not controllable independently, the roll can be controlled by adjusting the magnetic moment along the pitch and yaw directions.

The oloid is a 3D shape defined by generator lines that connect two identical, perpendicular circles [19] as shown in Figure 3. These generator lines serve as fundamental structural elements, creating the oloid's surface. The shape is discretized along an arc length parameter, $t$, where each value of $t$ corresponds to a unique point on circle 1 ($P_1$), and a corresponding point on circle 2 ($P_2$). The generator line is formed by connecting corresponding points $P_1$ and $P_2$. To fully define the oloid, the arc length parameter $t$ is constrained to the range $\frac{2\pi}{3} \leq t \leq \frac{2\pi}{3}$ for both circles. As the oloid rolls on a horizontal surface, each generator line sequentially makes contact with the surface, ensuring smooth motion. The line in contact at any given moment dictates the pose of the oloid, meaning that the existence of a generator line directly impacts the achievable range of motion.

To quantify how closely a shape adheres to the geometrical properties of a full oloid, we defined a term "oloidicity". This was determined by the range of $t$ values and the completeness of the generator lines. We define the completeness of generator lines by a function $g(t)$, where:

$$g(t) = \frac{\text{Length of generator line at t}}{r\sqrt{3}} \tag{1}$$

For a full oloid, $g(t) = 1$ for all $t$, whereas for partial oloids, $0 \leq g(t) < 1$. The oloidicity metric is therefore given by:

$$\text{Oloidicity} = \frac{\int_{-2\pi/3}^{2\pi/3}\int_{-2\pi/3}^{2\pi/3} g(t_1,t_2)dt_1dt_2}{(4\pi/3)^2} \tag{2}$$

This integral normalizes generator line completeness over the surface area, providing a quantitative measure of oloidicity across different hybridized shapes. A full oloid is achieved when $t$ spans the full range for both circles, while a partial oloid has a reduced range, limiting its contact points with the rolling surface.

### C. Magnetic Manipulation System

While this approach can be applied to a wide range of devices that are manipulated by magnetic fields (including

wireless capsule endoscopes), we adopt the MFE platform from previous work by [9] and [8] to prove the principle of operation.

The MFE platform (Figure 1) is a robotically controlled magnetic endoscope system comprised of a KUKA LBR, 7-DoF robotic manipulator which has a large cylindrical external permanent magnet (EPM) mounted as the end effector, a tethered magnetic endoscope with an embedded internal permanent magnet (IPM) and a real-time endoscope localization system.

The magnetic manipulation of the MFE is achieved by adjusting the pose of the EPM in 6 DoF which imparts magnetic force and torques onto the IPM allowing for the MFE to be pulled and steered through the GI tract in 5-DOF. On-board sensors and a complex localization algorithm [20] are used to obtain 6-DOF real-time pose feedback of the MFE in order to attain effective control. This enables the user to successfully navigate the GI tract with the endoscope using just a joystick as an input.

### *D. Magnetic Field Control*

The magnetic field control method presented here utilizes the dipole-dipole model and is based on [8], [9], [20] where full derivations can be found. The dipole moments of the EPM and the IPM are denoted as $\mathbf{m_E} \in \mathbb{R}^3$ and $\mathbf{m_I} \in \mathbb{R}^3$ respectively, and their positions as $\mathbf{p_E} \in \mathbb{R}^3$ and $\mathbf{p_I} \in \mathbb{R}^3$. All points and vectors are represented in the global frame. The input to this portion of the control is a desired rotation matrix of the IPM which is converted into a vector representing the desired IPM heading, $\hat{\mathbf{m}}_{\mathbf{I_d}}$. From the desired IPM heading, the required torque can be calculated based on the heading error ($\hat{\mathbf{m}}_{\mathbf{I}} \times \hat{\mathbf{m}}_{\mathbf{I_d}}$) where the magnitude is the angle between the two vectors.

Given a magnetic field $\mathbf{B_E}$ generated by the EPM, Maxwell's force and torque equations can be rewritten to represent the magnetic force $\mathbf{f}$ and torque $\boldsymbol{\tau}$ on the IPM.

$$\mathbf{f} = (\mathbf{m_I} \cdot \nabla)\mathbf{B_E} \tag{3}$$

$$\boldsymbol{\tau} = \mathbf{m_I} \times \mathbf{B_E} \tag{4}$$

The robot arm is controlled in joint space and has generalized coordinates denoted by $\mathbf{q} \in \mathbb{R}^7$. The relationship between the twist of the EPM which is mounted as the robot's end effector and the robot's joint velocities can be linearized using the robot's geometric Jacobian $J_R(\mathbf{q}) \in \mathbb{R}^{6\times7}$ as follows:

$$\begin{bmatrix} \dot{\mathbf{p}}_{\mathbf{E}} \\ \boldsymbol{\omega}_{\mathbf{E}} \end{bmatrix} = J_R(\mathbf{q})\,\dot{\mathbf{q}} \tag{5}$$

Due to the magnetic symmetry explained, we know that any rotation in $\boldsymbol{\omega}_{\mathbf{E}}$ along the EPM's magnetization axis will not affect the EPM's dipole moment $\hat{\mathbf{m}}_{\mathbf{E}}$ and therefore we can define the EPM's Jacobian, $J_E(\mathbf{q})$ as:

$$\begin{bmatrix} \dot{\mathbf{p}}_{\mathbf{E}} \\ \dot{\hat{\mathbf{m}}}_{\mathbf{E}} \end{bmatrix} = \begin{bmatrix} \mathbb{I}_3 & \mathbb{O}_3 \\ \mathbb{O}_3 & S(\hat{\mathbf{m}}_{\mathbf{E}})^T \end{bmatrix} J_R(\mathbf{q})\,\dot{\mathbf{q}} = J_E(\mathbf{q})\,\dot{\mathbf{q}} \tag{6}$$

where $\mathbb{I}_3$ is a 3x3 Identity matrix, $\mathbb{O}_3$ is a 3x3 zero matrix and $S()$ is the skew-symmetric form of the cross-product compensating for the symmetries in the magnetic field. The linearized form of the dipole-dipole model is therefore:

$$\begin{bmatrix} \dot{\mathbf{f}} \\ \dot{\boldsymbol{\tau}} \end{bmatrix} = \begin{bmatrix} \frac{\partial \mathbf{F_m}}{\partial \mathbf{p}} & \frac{\partial \mathbf{F_m}}{\partial \hat{m}_{\mathbb{E}}} & \frac{\partial \mathbf{F_m}}{\partial \hat{m}_{\mathbf{I}}} \\ \frac{\partial \tau_{\mathbf{m}}}{\partial \mathbf{p}} & \frac{\partial \tau_{\mathbf{m}}}{\partial \mathrm{m_E}} & \frac{\partial \tau_{\mathrm{m}}}{\partial \mathrm{m_I}} \end{bmatrix} \begin{bmatrix} \dot{\mathbf{p}} \\ \dot{\hat{\mathbf{m}}}_{\mathbf{E}} \\ \dot{\hat{\mathbf{m}}}_{\mathbf{I}} \end{bmatrix} \tag{7}$$

$$= J_f(\mathbf{p}, \mathbf{m_E}, \mathbf{m_I}) \begin{bmatrix} \dot{\mathbf{p}} \\ \dot{\hat{\mathbf{m}}}_{\mathbf{E}} \\ \dot{\hat{\mathbf{m}}}_{\mathbf{I}} \end{bmatrix} \tag{8}$$

where $\mathbf{p} = \mathbf{p_I} - \mathbf{p_E}$. Assuming the pose of the IPM remains constant, Equation 7 can be reduced to:

$$\begin{bmatrix} \dot{\mathbf{f}} \\ \dot{\boldsymbol{\tau}} \end{bmatrix} = J_f(\mathbf{p}, \mathbf{m_E}, \mathbf{m_I}) \begin{bmatrix} \dot{\mathbf{p}}_E \\ \dot{\hat{\mathbf{m}}}_{\mathbf{E}} \end{bmatrix} \tag{9}$$

The Jacobian $J_f$ is computed at every time step to ensure that the local linearization of the dipole-dipole model and the constant IPM pose remain locally valid assumptions. The overall control function can be defined as follows:

$$\begin{bmatrix} \dot{\mathbf{p}}_E \\ \dot{\hat{\mathbf{m}}}_{\mathbf{E}} \end{bmatrix} = J_f^{\dagger} \boldsymbol{pid}\left( \begin{bmatrix} \dot{\mathbf{f}} \\ \dot{\boldsymbol{\tau}} \end{bmatrix} \right) \tag{10}$$

The computation of the pseudoinverse of the Jacobian, $J_f^{\dagger}$ is then carried out by means of weighted/damped least squares algorithm shown in [8]. The angular and linear motions of the EPM are then transformed into desired changes in robot joint angles $\dot{\boldsymbol{q}} \in \mathbb{R}^7$ using the following:

$$\dot{\mathbf{q}} = J_f^{\dagger} \mathbf{W_a} \begin{bmatrix} \dot{\mathbf{p}}_{\mathbf{E}} \\ \dot{\hat{\mathbf{m}}}_{\mathbf{E}} \end{bmatrix} \tag{11}$$

Where $\mathbf{J}^{\dagger} \in \mathbb{R}^{7\times6}$ is the pseudoinverse of the robot's Jacobian, $\mathbf{W_a} \in \mathbb{R}^{6\times6}$ is a suitable weighting matrix. The desired changes in joint angles are fed to the robot controller for the robot to calculate the required inverse kinematics and to perform the necessary motion.

### *E. Integration into a Robotic Colonoscopy Platform and Pre-clinical Evaluation*

To accommodate the ancillary components of a magnetic endoscope, a full oloid would need to be scaled beyond a clinically relevant size. In contrast, a cylinder is optimal for component integration but lacks controllable roll. Consequently, the functional areas of the oloid were evaluated to facilitate the development of a hybrid design.

The endoscope had to be comparable in size to other magnetically manipulated endoscopes, such as the cylindrical MFE endoscope, which measures $20 \times 20 \times 40$ mm [21]. It had to also incorporate magnetic manipulation and localization capabilities, requiring a magnet core and a localization system. Additionally, the design had to support white-light imaging (WLI) and essential endoscopic functions, including insufflation, irrigation, and camera cleaning (see Figure 1). Safety considerations included smooth edges to prevent damage to the colon wall and waterproofing to protect internal components. The endoscope also had to be sensor-agnostic,

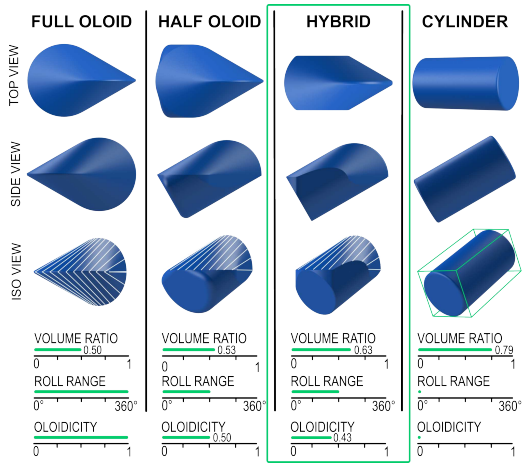


Fig. 4. **Summary table for hybrid oloid-cylinder endoscope designs**: oloid generator lines are shown in white in iso view. Volume ratio, roll range and oloidicity are defined in the text.

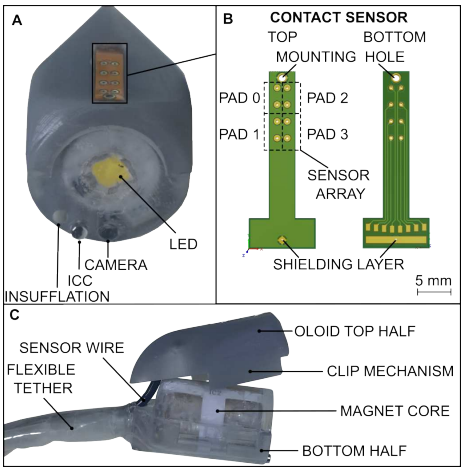


Fig. 5. **Oloid Magnetic Endoscope (OME)**: **(A)** Front view of OME showing the camera, LED, Irrigation, and camera cleaning (ICC) and insufflation, **(B)** Top and bottom view of the contact sensor PCB and **(C)** Side view of OME showing the clip mechanism and magnet core with top half unclipped.

to allow compatibility with various submucosal visualization sensors. Finally, the design had to achieve a minimum range of motion of $\pm 25^\circ$ in roll, yaw, and pitch.

### *F. Endoscope Shape Optimization*

To compare component integration across designs, we scaled each design to fit within a $20 \times 20 \times 40$ mm bounding box and used a dimensionless volume ratio, which represents the shape's volume relative to the volume of the bounding box (green box in Figure 4). Figure 4 illustrates a sample of the designs considered and the trade-offs made to achieve a hybrid design that meets the design requirements.

The full oloid design provided the largest roll range but had the lowest volume ratio of 0.50. In contrast, the cylindrical design achieved the highest volume ratio of 0.79, indicating that the full oloid endoscope would need to be approximately 1.6 times larger than the cylinder to achieve the same internal volume. By limiting the controllable roll range to 180°, the half oloid design improved the volume ratio to 0.53. This was further increased to 0.63 by the hybrid (oloid and cylinder) design while maintaining the controllable roll range of the half oloid design. Since the internal components to be integrated into the endoscope are primarily cylindrical, the size of the largest internal cylinder that could fit within each design was an important consideration. To accommodate a given cylindrical component, the full oloid, half oloid, and hybrid designs would need to be approximately 10, 5, and 3 times larger, respectively, than the cylinder.

When comparing the half oloid design to the hybrid design, although the number of generator lines remained the same, some were reduced in length to produce a smaller overall cross-section. This modification is reflected in the oloidicity values. The hybrid design was selected overall because it was the closest to the cylinder in terms of cross-section and volume ratio while maintaining a sufficient roll range to achieve the desired sweeping motions. In this case, the design constraints significantly limited the parameter space, making formal optimization unnecessary; however, as a fully defined mathematical concept, the shape could readily be optimized.

### *G. Contact Sensors*

Our vision is to use this device for submucosal visualization, such sensors usually rely on constant contact with the tissue. Therefore, here we integrated a multi-point contact sensor to evaluate and characterize our approach. On its upper centerline, the endoscope provides the largest and flattest area (shown in Figure 5(A)). This area provides the best conditions for the integration of this sensing modality. To provide in situ information on contact of this surface, contact sensors were integrated into a 4 x 10 $mm^2$ area in this location. The sensor is based on capacitive measurement using eight electrodes distributed in a 2 x 4 pattern over this area. Capacitive sensing allows for very thin electrodes with low volume profile. The electrodes are manufactured as flexible printed circuit board of 10 mm width, 0.1 mm thickness and 26 mm length, including solder pads inside the endoscope (Figure 5(B)). The sensor's transducers and processing unit were implemented at the distal part of the system at the robot's base. The electrode array was placed in a notch prepared for the sensor and aligned using a mounting hole on the PCB. The sensor system is based on the method presented in [22]. Sensor values were published to the robot's robot operating system (ROS) network. The sensor array was split into four quarters; the combined readings from the electrode provide binary information of contact for each quarter section at a rate of 50 Hz.

### *H. Endoscope Manufacture*

The 3D endoscope shell was printed in resin on the Form3 3D printer (FormLabs) in three parts, the top half, the bottom right and the bottom left shown in Figure 5(C). The magnet core, camera, ICC, and insufflation tubes were carefully

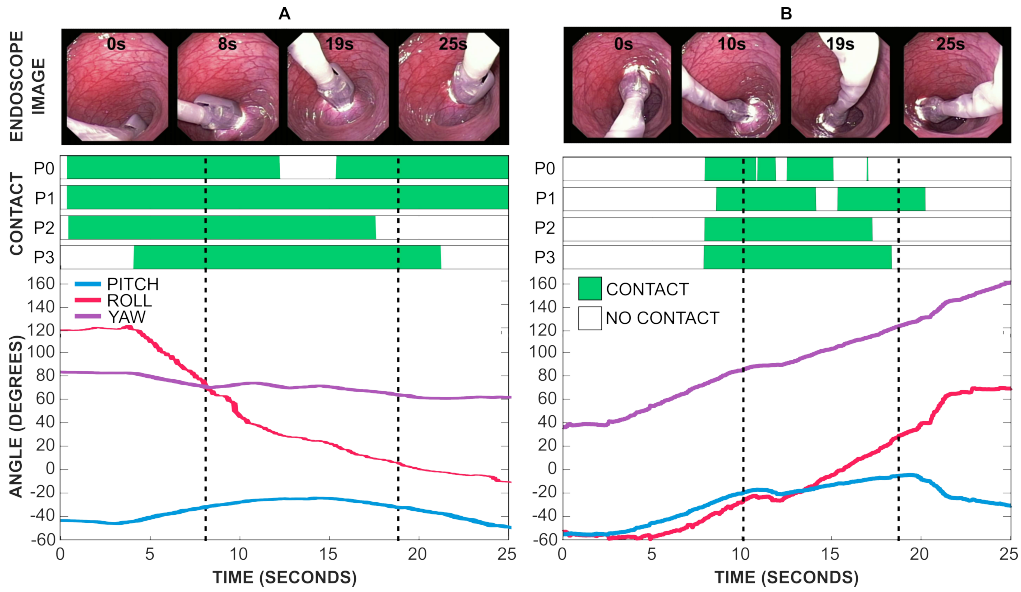


Fig. 6. **In vivo OME results**: Contact sensor data plotted over time with orientation data from the endoscope's localization and selected scenes from the standard endoscopes video stream and OME orientation data during a **(A)** sweeping and **(B)** rolling motion in vivo.

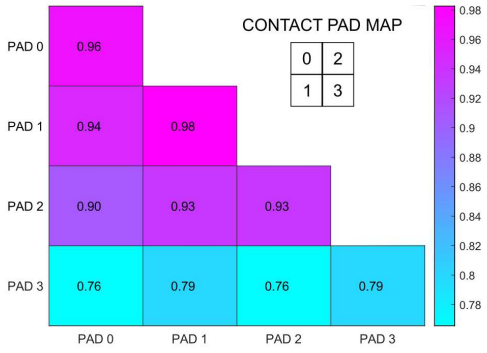


Fig. 7. **Sweep motion in vivo contact data**: Average contact data for all four contact pads during in vivo sweeping motions over a 100° roll range.

inserted into their positions before sealing the two bottom halves together. The endoscope was designed to be sensor-agnostic, with an interchangeable or "hot swappable" feature so that a singular base could form the test bed for multiple sensor types and designs. This was done to reduce waste, but may have utility in the clinical setting, where the user can have the option to swap between sensor types in the middle of a procedure. For this reason, the bottom half had to be fully encapsulated for waterproofing. This was done by creating small ventilation holes in the endoscope's shell before filling all the gaps with high viscosity cyanoacrylate (Permabond 4c40). By doing this, the mechanical connection between the two halves does not have to be watertight, significantly reducing the complexity of this portion of the design. The mechanical connection between the two halves leverages the 3D printed structure with an integrated clip mechanism on the side of the endoscope (shown in Figure 5(C)) which is easy to clip on and off, but secure enough to stay on during use. The sensor wire for the contact sensors was fed through a channel in the tether using a biopsy tool as shown in Figure 5(C).

The resulting oloid magnetic endoscope (OME) design shown in Figure 5 meets all the design requirements set out in at the beginning of this section and has overall dimensions of 20 x 20 x 35 mm.

## III. Results and Discussion

### A. In Vivo Demonstration of Sweeping and Rolling Motions

With an endoscope that fulfilled all the necessary design criteria, in vivo experiments were carried out to showcase the system's potential for clinical use. A porcine model was selected for these tests due to the significant similarity between a pig's gastrointestinal anatomy and that of a human.

The experiments were carried out on a 39 kg large white female pig under general anesthesia, following this procedure. These trials were authorized by the home office (UK) under license (procedure project license: PF5151DAF) and complied with the animal (scientific procedures) act 1986.

After thoroughly cleansing the colon with several enemas, the OME was inserted through the rectum and advanced approximately 20 cm into the colon. This length offered a long, straight section of the bowel suitable for experimentation. The OME's auxiliary components were employed for colon distension and irrigation as needed.

The primary goals of these trials were to prove that the OME could successfully roll in vivo and execute clinically relevant motions for contact-based sensing (Supplementary Video). To validate this, two experiments were devised. The first involved a sweeping motion over the upper half of the colon surface (Figure 6(A)), while the second focused on a pure rolling motion within a $\pm 50°$ range (Figure 6(B)). Each experiment was conducted five times. These motions were performed using open-loop joy-stick control. To provide

proof of contact, the visual evidence was backed up with the contact-sensing data, which monitored contact with the colon wall throughout the experiments.

Figure 6 shows the sweeping and rolling motions along with the contact data processed as binary measurements of contact/no-contact and the OME's orientation data. A range of 100° roll was achieved during the sweeping motion. Contact data was analyzed over 2 repetitions, showing that contact was maintained on all pads 74% of the time, with mean contact on individual pads being 92%. To analyze what subsections of the potential sensor head area remain in contact during roll motion, combined contact of two pads was analyzed. Figure 7 shows the matrix of contact data over the sweeping motion for all contact pads. The strongest correlation was seen on the pads 0 and 1 (left side) and the weakest on pads 0 and 3. Thus, maintaining the top-left to bottom right diagonal in contact seems to be most difficult. However, we believe that these results can be improved if the contact data is used in the feedback control loop for the OME and a properly integrated sensor head will cover less than the tested surface.

## IV. Conclusion

In this work we were able to present a design using the oloid shape that met all the design requirements of an endoscope and perform sweeping motions whilst maintaining a contact area of 4mm x 10mm area throughout 74% of the motion.

With this, we can say that the use of the oloid shape as a roll recovery method was successful. This method of roll recovery presents a novel way to improve position control, scope stabilization, and surface scanning to magnetically manipulated endoscopes without requiring additional power and is therefore applicable to both tethered and untethered applications.

The oloid shape can be scaled up or down to allow this method to be applied to a range of applications.

Future work will look at integrating submucosal visualization sensors such as ultrasound and Terahertz sensors in the pursuit of 'virtual biopsy' and to include this data in the feedback control in order to achieve higher contact percentages. Another avenue to explore would be developing more advanced control algorithms for roll control to enable complex procedures such as endoscopic submucosal dissection (ESD).

## References


[1] Yue Xi, Yue Xi, Yue Xi, Pengfei Xu, Pengfei Xu, and Pengfei Xu, "Global colorectal cancer burden in 2020 and projections to 2040."

[2] C.-K. Yeung, J. L. Cheung, and B. Sreedhar, "Emerging next-generation robotic colonoscopy systems towards painless colonoscopy," vol. 20, no. 4, pp. 196–205. [Online]. Available: https://onlinelibrary.wiley.com/doi/abs/10.1111/1751-2980.12718

[3] J. W. Rey, R. Kiesslich, and A. Hoffman, "New aspects of modern endoscopy," vol. 6, no. 8, pp. 334–344. [Online]. Available: https://www.ncbi.nlm.nih.gov/pmc/articles/PMC4133412/

[4] G. Iddan, G. Meron, A. Glukhovsky, and P. Swain, "Wireless capsule endoscopy," vol. 405, no. 6785, pp. 417–417. [Online]. Available: https://www.nature.com/articles/35013140

[5] N. Shamsudhin, V. I. Zverev, H. Keller, S. Pane, P. W. Egolf, B. J. Nelson, and A. M. Tishin, "Magnetically guided capsule endoscopy," vol. 44, no. 8, pp. e91–e111. [Online]. Available: https://onlinelibrary.wiley.com/doi/abs/10.1002/mp.12299

[6] S. Nouda, K. Ota, and K. Higuchi, "Retrograde colon capsule endoscopy with the self-propelling capsule endoscope: The first human trial (with videos)," vol. 30, no. 1, pp. 117–118. [Online]. Available: https://onlinelibrary.wiley.com/doi/abs/10.1111/den.12969

[7] A. Mahoney and J. J. Abbott, "Generating Rotating Magnetic Fields With a Single Permanent Magnet for Propulsion of Untethered Magnetic Devices in a Lumen."

[8] J. W. Martin, B. Scaglioni, J. C. Norton, V. Subramanian, A. Arezzo, K. L. Obstein, and P. Valdastri, "Enabling the future of colonoscopy with intelligent and autonomous magnetic manipulation," vol. 2, no. 10, pp. 595–606. [Online]. Available: https://www.nature.com/articles/s42256-020-00231-9

[9] J. C. Norton, P. R. Slawinski, H. S. Lay, J. W. Martin, B. F. Cox, G. Cummins, M. P. Desmulliez, R. E. Clutton, K. L. Obstein, S. Cochran, and P. Valdastri, "Intelligent magnetic manipulation for gastrointestinal ultrasound," vol. 4, no. 31, p. eaav7725. [Online]. Available: https://www.science.org/doi/10.1126/scirobotics.aav7725

[10] X. Wang, V. Seetohul, R. Chen, Z. Zhang, M. Qian, Z. Shi, G. Yang, P. Mu, C. Wang, Z. Huang, Q. Zhou, H. Zheng, S. Cochran, and W. Qiu, "Development of a Mechanical Scanning Device With High-Frequency Ultrasound Transducer for Ultrasonic Capsule Endoscopy," vol. 36, no. 9, pp. 1922–1929.

[11] Y. Qiu, Y. Huang, Z. Zhang, B. F. Cox, R. Liu, J. Hong, P. Mu, H. S. Lay, G. Cummins, M. P. Y. Desmulliez, E. Clutton, H. Zheng, W. Qiu, and S. Cochran, "Ultrasound Capsule Endoscopy With a Mechanically Scanning Micro-ultrasound: A Porcine Study," vol. 46, no. 3, pp. 796–804. [Online]. Available: https://www.umbjournal.org/article/S0301-5629(19)31623-0/fulltext

[12] P. Wang, P. Liu, J. R. G. Brown, T. M. Berzin, G. Zhou, S. Lei, X. Liu, L. Li, and X. Xiao, "Lower Adenoma Miss Rate of Computer-Aided Detection-Assisted Colonoscopy vs Routine White-Light Colonoscopy in a Prospective Tandem Study," *Gastroenterology*, vol. 159, no. 4, pp. 1252–1261.e5, Oct. 2020, publisher: Elsevier. [Online]. Available: https://www.gastrojournal.org/article/S0016-5085(20)34820-4/fulltext

[13] S. H. Kim and H. J. Chun, "Capsule Endoscopy: Pitfalls and Approaches to Overcome," vol. 11, no. 10, p. 1765. [Online]. Available: https://www.mdpi.com/2075-4418/11/10/1765

[14] B. F. Cox, F. Stewart, H. Lay, G. Cummins, I. P. Newton, M. P. Y. Desmulliez, R. J. C. Steele, I. Nthkeä, and S. Cochran, "Ultrasound capsule endoscopy: Sounding out the future," vol. 5, no. 9, pp. 9–9. [Online]. Available: https://atm.amegroups.com/article/view/14711

[15] Y. Li, Z. Zhu, J. J. Chen, J. C. Jing, C.-H. Sun, S. Kim, P.-S. Chung, and Z. Chen, "Multimodal endoscopy for colorectal cancer detection by optical coherence tomography and near-infrared fluorescence imaging," vol. 10, no. 5, pp. 2419–2429. [Online]. Available: https://www.ncbi.nlm.nih.gov/pmc/articles/PMC6524571/

[16] S. Choi, J. Kim, H. Jeon, C. Kim, and E.-Y. Park, "Advancements in photoacoustic detection techniques for biomedical imaging," *npj Acoustics*, vol. 1, no. 1, p. 1, Mar. 2025, publisher: Nature Publishing Group.

[17] G. Reese, C. Reid, R. Goldin, M.-A. Tran-Dang, A. Fitzgerald, P. Tekkis, V. P. Wallace, and V. P. Wallace, *Using Terahertz Pulsed Imaging (TPI) to Identify Colonic Pathology.* IEEE.

[18] L. Barducci, J. C. Norton, S. Sarker, S. Mohammed, R. Jones, P. Valdastri, and B. S. Terry, "Fundamentals of the gut for capsule engineers," vol. 2, no. 4, p. 042002. [Online]. Available: https://doi.org/10.1088/2516-1091/abab4c

[19] H. Dirnbock and H. Stachel, "The Development of the Oloid," vol. 1.

[20] A. Z. Taddese, P. R. Slawinski, M. Pirotta, E. De Momi, K. L. Obstein, and P. Valdastri, "Enhanced real-time pose estimation for closed-loop robotic manipulation of magnetically actuated capsule endoscopes," vol. 37, no. 8, pp. 890–911. [Online]. Available: https://doi.org/10.1177/0278364918779132

[21] N. G. Kim, N. J. Greenidge, J. Davy, S. Park, J. H. Chandler, J.-H. Ryu, and P. Valdastri, "External Steering of Vine Robots via Magnetic Actuation." [Online]. Available: https://www.liebertpub.com/doi/abs/10.1089/soro.2023.0182

[22] H. Alagi, S. E. Navarro, M. Mende, and B. Hein, "A versatile and modular capacitive tactile proximity sensor," in *2016 IEEE Haptics Symposium (HAPTICS)*, pp. 290–296.